This is a repository copy of *Impact of interface energetic alignment and mobile ions on charge carrier accumulation and extraction in p-i-n perovskite solar cells*.

White Rose Research Online URL for this paper:
https://eprints.whiterose.ac.uk/202174/

Version: Published Version

RESEARCH ARTICLES

W. Xu, L. J. F. Hart, B. Moss,
P. Caprioglio, T. J. Macdonald,
F. Furlan, J. Panidi, R. D. J. Oliver,
R. A. Pacalaj, M. Heeney,
N. Gasparini, H. J. Snaith,
P. R. F. Barnes,*
J. R. Durrant* 2301102

Impact of Interface Energetic Alignment and Mobile Ions on Charge Carrier Accumulation and Extraction in p-i-n Perovskite Solar Cells
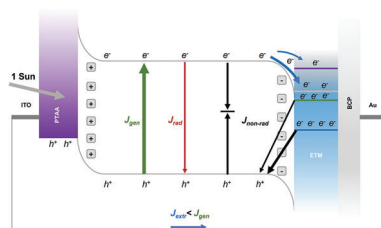
Operando photoluminescence measurements and drift-diffusion simulations are used to investigate the performance of perovskite solar cells with different electron transport materials (ETMs). It is demonstrated that the energetic alignment at the perovskite/ETM interface strongly influences the balance between electronic charge extraction and recombination. Moreover, electronic charge accumulation is observed at short-circuit, which is attributed to field screening by mobile ions.

Impact of Interface Energetic Alignment and Mobile Ions on Charge Carrier Accumulation and Extraction in p-i-n Perovskite Solar Cells

Weidong Xu, Lucy J. F. Hart, Benjamin Moss, Pietro Caprioglio, Thomas J. Macdonald, Francesco Furlan, Julianna Panidi, Robert D. J. Oliver, Richard A. Pacalaj, Martin Heeney, Nicola Gasparini, Henry J. Snaith, Piers R. F. Barnes,* and James R. Durrant*

Understanding the kinetic competition between charge extraction and recombination, and how this is impacted by mobile ions, remains a key challenge in perovskite solar cells (PSCs). Here, this issue is addressed by combining operando photoluminescence (PL) measurements, which allow the measurement of real-time PL spectra during current–voltage (J–V) scans under 1-sun equivalent illumination, with the results of drift-diffusion simulations. This operando PL analysis allows direct comparison between the internal performance (recombination currents and quasi-Fermi-level-splitting (QFLS)) and the external performance (J–V) of a PSC during operation. Analyses of four PSCs with different electron transport materials (ETMs) quantify how a deeper ETM LUMO induces greater interfacial recombination, while a shallower LUMO impedes charge extraction. Furthermore, it is found that a low ETM mobility leads to charge accumulation in the perovskite under short-circuit conditions. However, this alone cannot explain the remarkably high short-circuit QFLS of over 1 eV which is observed in all devices. Instead, drift-diffusion simulations allow this effect to be assigned to the presence of mobile ions which screen the internal electric field at short-circuit and lead to a reduction in the short-circuit current density by over 2 mA cm^{-2} in the best device.

1. Introduction

Over the past decade, organic–inorganic metal halide perovskite solar cells (PSCs) have made remarkable progress, with optimized devices achieving a 26.0% and 31.3% power conversion efficiency (PCE) for single-junction cells and monolithic perovskite/silicon tandem cells, respectively.[1,2] This progress can be attributed to the rapid evolution of materials and device engineering techniques, which have allowed the field to obtain both high-quality bulk perovskites with low defect densities and contact materials which facilitate efficient charge-extraction. Nevertheless, the processes underlying charge extraction, namely charge transport within the perovskite layer, charge transfer from the perovskite layer to its contacts and charge transport through the contact materials to the electrodes, have received relatively little attention.[3–7] In a PSC, photogenerated charges must travel to the interfaces and

W. Xu, L. J. F. Hart, B. Moss, T. J. Macdonald, F. Furlan, J. Panidi,
R. A. Pacalaj, M. Heeney, N. Gasparini, J. R. Durrant
Department of Chemistry and Centre for Processable Electronics
Imperial College
London W12 0BZ, UK
E-mail: j.durrant@imperial.ac.uk

L. J. F. Hart, R. A. Pacalaj, P. R. F. Barnes
Department of Physics and Centre for Processable Electronics
Imperial College
London SW7 2AZ, UK
E-mail: piers.barnes@imperial.ac.uk

P. Caprioglio, R. D. J. Oliver, H. J. Snaith
Department of Physics
University of Oxford
Clarendon Laboratory
Parks Road, Oxford OX1 3PU, UK

T. J. Macdonald
School of Engineering and Materials Science
Queen Mary University of London
London E1 4NS, UK

R. D. J. Oliver
Department of Physics and Astronomy
University of Sheffield
Hounsfield Road, Sheffield S3 7RH, UK

J. R. Durrant
SPECIFIC IKC
College of Engineering
Swansea University
Bay Campus, Fabian Way, Swansea, Wales SA1 8EN, UK

be transferred to the interlayers before finally being collected by the external circuit. Prior to charge collection, it is possible for carriers to undergo recombination, such as trap-assisted non-radiative recombination, band-to-band radiative recombination, and surface/interface non-radiative recombination, with non-radiative loss pathways often limiting the performance of scalable devices.[8,9] As a result, a key determinant of device performance is the kinetic competition between these recombination processes and charge extraction, making it necessary to understand their relative rates in order to develop PSCs further toward commercial applications. Most studies which investigate recombination dynamics in PSCs measure devices at open-circuit (OC),[10–14] and thus in the absence of net charge extraction. In this study, we extend upon this by probing these processes in complete devices under different biases. As such, we can investigate whether conclusions reached under OC conditions are valid under actual device operating conditions.

When considering charge extraction in PSCs, a key factor to take into consideration is the screening of the built-in electric field by mobile ions, an effect which has been demonstrated both experimentally and using device simulations.[15–17] This ion induced modulation of the internal electric field is thought to be one of the key factors causing current-voltage (J–V) hysteresis and the light soaking effect in PSCs,[16,18–21] and has been reported to reduce their stabilized photocurrent output,[22] as well as creating a discrepancy between time-dependent measurements and stabilized device performance.[23,24] Herein, we use operando photoluminescence (PL) spectroscopy (described further below) to demonstrate an additional consequence of ionic shielding; significant charge accumulation in the perovskite layer, even under short-circuit (SC) conditions. Numerical simulations are employed to demonstrate that this SC charge accumulation is likely to be a direct consequence of ion-induced field screening, which results in the transport of electrons and holes to the device contacts being driven by diffusion, rather than drift. Consequently, this field screening leads to higher steady-state carrier populations in the perovskite under SC conditions compared to the case when the effects of mobile ions are neglected.

Another important factor when optimizing devices for efficient charge extraction is the choice of contact layers. For p-i-n PSCs, the electron transport material (ETM) is particularly important. Several studies have reported that the properties of the ETMs used in the most efficient p-i-n PSCs, such as [6,6]-phenyl-C61-butyric acid methyl ester ($PC_{60}BM$) and C_{60}, are not ideal, as they either contribute to a high series resistance or cause non-negligible surface recombination if their interface with the perovskite is not appropriately passivated.[25,26] In addition, in state-of-the-art wide-bandgap PSCs (which are used as the top cells in tandem solar cells, and in indoor applications), the energetics of the ETM's lowest unoccupied molecular orbital (LUMO) and the perovskite's conduction band are not well matched, which leads to additional surface recombination.[27,28] Therefore, understanding how ETM properties, in particular their LUMO level and electron mobility, affect charge accumulation, transfer and extraction dynamics is crucial to further improve p-i-n PSCs. To elucidate the impact of these properties on charge extraction, we investigated methylammonium-free PSCs with four different ETMs, which were selected to cover a range of LUMO values. Here, methylammonium-free per-ovskites were chosen since they show better stability and compatibility with tandems or flexible substrates than those containing methylammonium.[27,29–32]

Steady-state PL spectroscopy has been widely used to examine the properties of perovskites by monitoring their radiative recombination. PL from perovskite devices results from the radiative, band-to-band recombination of electrons and holes in the perovskite layer making its intensity an assay of the densities of these charges.[33–35] Thus, once the integrated PL spectrum is evaluated, it is possible to calculate the PL quantum yield (PLQY), radiative recombination current (J_{rad}) and quasi-Fermi-level-splitting (QFLS) using the following equations:[33,36]

$$\text{QFLS} = k_B\, T \cdot \ln\left(\frac{J_{\text{rad}}}{J_{0,\text{rad}}}\right) = k_B\, T \cdot \ln\left(\text{PLQY}\,\frac{J_{\text{gen}}}{J_{0,\text{rad}}}\right) \tag{1}$$

where J_{rad} is the measured total radiative equivalent current density, J_{gen} is the measured photogeneration current density, $J_{0,rad}$ is the dark radiative recombination current density determined from the integral of the external quantum efficiency and the black body spectrum (see Figure S1, Supporting Information), k_B is Boltzmann's constant and T is the temperature. This method allows one to compare the internal bulk QFLS to the external open-circuit voltage (V_{OC}) and has been used extensively as an assay of the dominant recombination mechanisms in PSCs at OC.[33,37,38] While most such studies have focused on understanding the origin of V_{OC} losses, a full understanding of PSC performance requires measurement of the QFLS across the J–V curve. In our previous studies, we have used the quenching of PL from OC to SC as a figure of merit to assess the charge extraction efficiency of PSCs.[34,35,39–41] Other reports have demonstrated the correlation between voltage-dependent PL and PSC performance.[4,42,43] In this work we build on these insights and introduce an operando PL measurement, similar to that used by Stolterfoht et al.,[4] but with a greater focus on measurements performed while the device is under operating conditions. This technique is based on measurement of absolute PL spectra whilst simultaneously performing a J–V scan under 1-sun equivalent illumination, as shown in **Figure 1**a. By calculating the QFLS and the various recombination currents, this technique allows us to monitor the accumulation, recombination, and extraction of photogenerated charge carriers across the J–V curve, and thus quantitively evaluate the relative impact of these processes upon device efficiency at a variety of applied voltages.

In the study herein, we report the observation of significant electronic charge accumulation at SC in all the devices measured, irrespective of the choice of ETM. Device modeling indicates that this electronic charge accumulation is caused by ionic screening of the built-in electric field. We then go on to investigate how changing the energetics and mobility of the ETM impacts upon device performance. Our results show that a negative energy offset from the perovskite's conduction band to the ETM's LUMO increases surface recombination losses at the perovskite/ETM interface, which reduces V_{OC}, while a positive energy offset leads to a reduction in electronic charge extraction efficiency, limiting short-circuit current density (J_{SC}) and fill factor (FF). Additionally, a low mobility ETM can cause additional electronic charge accumulation in the perovskite bulk under SC conditions. Overall, our
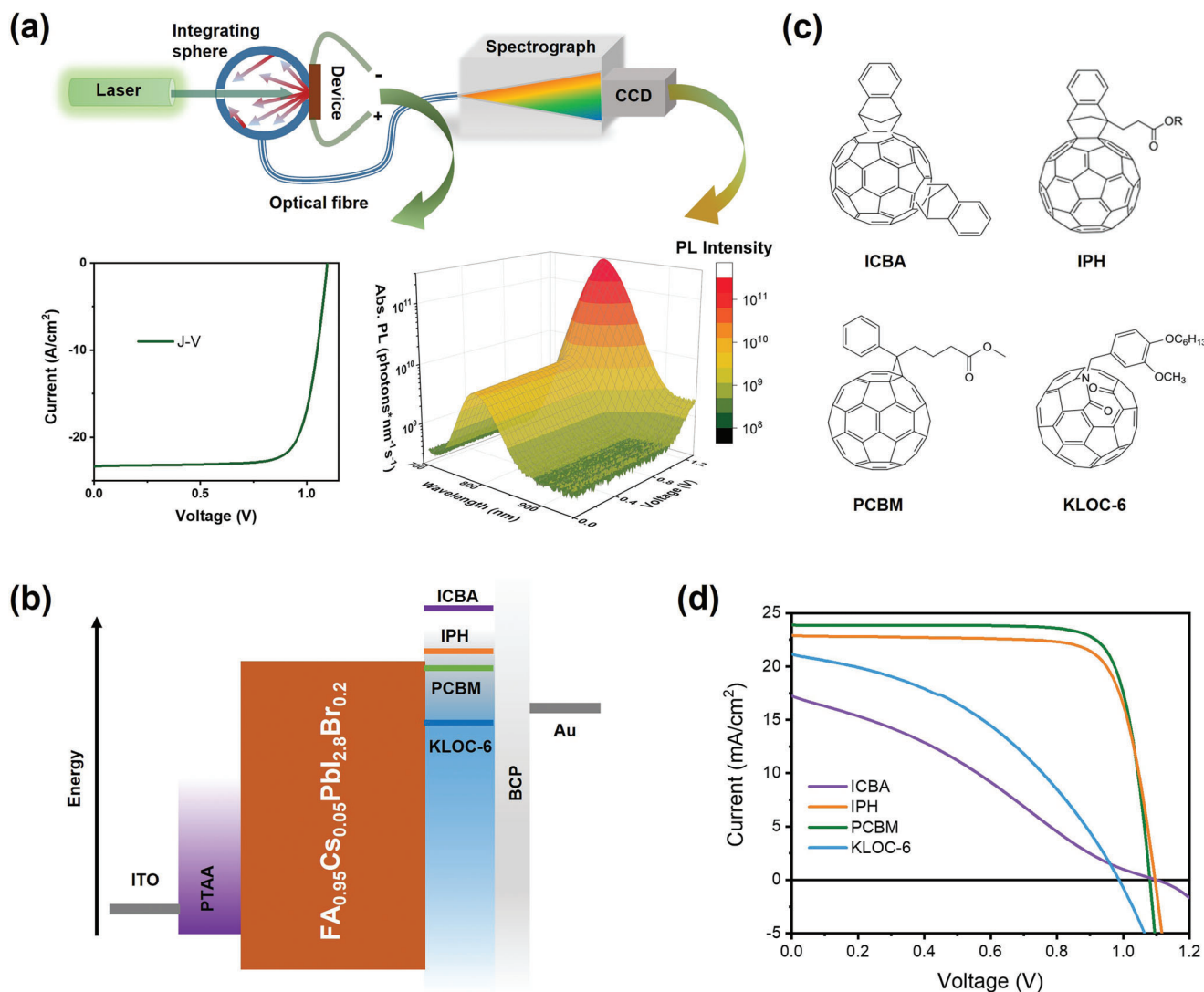
ADVANCED
SCIENCE NEWS
www.advancedsciencenews.com

ADVANCED
ENERGY
MATERIALS
www.advenergymat.de

Figure 1. a) Schematic drawing of operando PL set-up. b) Flat-band energy alignment with different ETM LUMOs.[44] c) Chemical structures of all fullerene-based electron transport materials. d) Device J–V performance, as obtained from the operando PL measurement under 1-sun equivalent 532 nm CW laser illumination. J–V scans were performed in the forward direction at a scan speed of 7 mV s^{-1}.

results explain and quantify how loss mechanisms in these devices are strongly influenced by both the perovskite/contact layer interfacial properties and the effects of ion migration.

2. Results

2.1. Device Structure

In this work, four p-i-n PSCs with the same device structure, but varied ETMs, were studied using operando PL spectroscopy, with the detailed experimental procedure given in Section 5. Figure 1b shows the flat-band energy alignment of these devices, which have the geometric structure ITO/PTAA/perovskite/ETM/BCP/Au: ITO is indium-doped tin oxide, PTAA is Poly[bis(4-phenyl)(2,4,6-trimethylphenyl)amine], perovskite is $FA_{0.95}Cs_{0.05}PbI_{2.8}Br_{0.2}$ (FA = formamidinium), and BCP is bathocuproine. The four ETMs used were ICBA, IPH,

Table 1. Summary of device J–V parameters from operando PL measurement and LUMO levels of ETMs.

ETM	J_{SC} [mA cm^{-2}]	V_{OC} [V]	FF	PCE [%]	LUMO [eV]
ICBA	17.2	1.10	0.30	5.68	−3.70
IPH	22.9	1.10	0.77	19.40	−3.79
PCBM	23.9	1.08	0.79	20.37	−3.82
KLOC-6	21.2	0.99	0.41	8.59	−4.04

PCBM, and KLOC-6. Their chemical structures are shown in Figure 1c and typical values of their electron affinity/LUMO are summarized in **Table 1** with the caveat that the absolute values of the electron affinity/LUMO of these materials vary across the literature, depending, for example, upon the measurement technique employed. Other factors, such as localized electronic states

extending into the bandgap due to structural impurity, or compositional disorder (tail states) can further complicate determination of absolute band edges.[45,46] Nevertheless, it has been consistently found that ICBA has the shallowest LUMO of the chosen ETM materials, followed by IPH, then PCBM and lastly KLOC-6.[44,47–50] Herein we use the energetic ordering determined by Willems et al. for all these ETMs.[44] As the method of square-wave voltammetry was used for all the samples, their relative LUMO levels can be compared with confidence.[44] Furthermore, it is usually found that the LUMO of PCBM lies slightly below the perovskite conduction band , meaning that devices with this ETM should be the closest to forming an Ohmic contact at the perovskite/ETM interface.[44,51,52]

2.2. Charge Transport Property of ETMs

We turn to investigate the electron transport properties of these ETMs. The method of space-charge-limited-current (SCLC) was first employed, in which the mobilities of the ETMs were determined by fitting J–V data from the electron-only devices, as illustrated in Figure S2, Supporting Information. The results follow the trend PCBM> IPH> ICBA> KLOC-6 with values of 2.66×10^{-4}, 4.44×10^{-5}, 3.38×10^{-5}, and 1.18×10^{-5} cm^2 V^{-1} s^{-1}, respectively. With this technique the mobility extracted is referred to as the vertical bulk mobility. We note that the absolute values determined using SCLC analysis also depend on the contact layer properties.[53,54] Therefore, as a cross check, we also measured the mobilities using thin-film transistors (TFTs), with the results shown in Figure S3, Supporting Information. Though much larger values were obtained from analyzing the TFT measurements, as is typical for this technique, the same trend in mobility was observed.

2.3. Photovoltaic Performance

J–V curves obtained during the operando PL measurement under continuous-wave (CW) 532 nm laser illumination, calibrated using the PCBM device to yield the same J_{SC} as measured under AM 1.5G, are shown in Figure 1d and summarized in Table 1. The PCBM device performs best, with the highest J_{SC} and FF of 23.9 mA cm^{-2} and 0.79, respectively and a V_{OC} of 1.08 V. Although the devices using ICBA and IPH show the highest V_{OC} of 1.10 V, compared to PCBM they have lower PCEs due to their lower J_{SC} values (22.9 mA cm^{-2} for IPH, 17.2 mA cm^{-2} for ICBA) and FFs (0.77 for IPH, 0.30 for ICBA). The KLOC-6 device has the lowest V_{OC} of 0.99 V, as well as a reduced J_{SC} and FF of 21.2 mA cm^{-2} and 0.41 respectively. Compared to ICBA, KLOC-6 still performs better due to its higher J_{SC} and FF. These parameters are comparable to those measured under simulated AM 1.5 irradiation, with J_{SC}'s cross checked by integration from the photovoltaic external quantum efficiency (EQE$_{PV}$) spectrum, as summarized in Figure S4 and Table S1, Supporting Information, with the PCE of the PCBM device being comparable to the reference values reported elsewhere in the literature for this device stack.[55,56] The trends in performance also agree qualitatively with the V_{OC} and J_{SC} trends observed in organic solar cells using these ETMs as acceptors.[44]

2.4. PLQY and Transient Optical Measurements

In order to understand the impact of energetic alignment on charge transfer at the perovskite/ETM interface, we employed steady-state and time-resolved PL (TRPL), as well as ultrafast transient absorption spectroscopy (TAS), on neat perovskite and perovskite/ETM bilayer films. **Figure 2**a shows the TRPL decay kinetics of the five samples. All decays appear biphasic, with a fast (few ns) phase followed by a slow (hundreds of ns) phase. As all the films were excited from the glass/perovskite interface and a low excitation fluence of 0.4 nJ cm^{-2} was used, we attribute the initial fast phase to charge trapping in the perovskite layer, in line with previous interpretations in the literature (this phase is suppressed at higher laser fluxes due to trap filling).[5,12] Considering the second phase, neat perovskite shows the slowest decay, followed by ICBA and IPH, while PCBM and KLOC-6 decay the fastest. As previously, the slow phase of the neat perovskite film is assigned to bulk recombination kinetics, while the acceleration of this phase in the bilayers is assigned to charge transport to the perovskite/ETM interface and subsequent charge transfer from the perovskite to the ETM (we note that, as the ETMs are undoped, there must be charge transfer from the perovskite to the ETM prior to surface recombination of an ETM electron with a perovskite hole).[5] As transport kinetics in the perovskite are expected to be independent of ETM, the faster decay of the second phase observed in the samples with PCBM and KLOC-6 is indicative of more efficient charge transfer at the perovskite/ETM interface, while the slower decay of this phase observed in IPH and ICBA suggests less complete charge transfer due to higher rates of back charge transfer from the ETM to the perovskite. This more efficient charge transfer for KLOC-6 and PCBM results in a higher proportion of surface rather than bulk recombination, consistent with the lower steady-state PLQY in these bilayers, as shown in Figure 2b. These findings are corroborated by TAS results in Figure S5, Supporting Information, where the band-edge photobleaching kinetics demonstrate a similar trend in decay rates as the TPRL kinetics. Due to the greater time resolution of the ultrafast measurement, we can discern that the KLOC-6 signal decays more rapidly than the PCBM signal, indicating that the deeper LUMO level of KLOC-6 increases the rate of charge transfer from the perovskite to the ETM.

2.5. Operando PL, QFLS and Electroluminescence

We now present the operando PL spectra of the full devices, which are summarized in **Table 2**. **Figure 3**a–d show the absolute PL spectra of the devices as the voltage is scanned from 0 to 1.3 V under 1-sun equivalent CW laser illumination, with the PLQY for each device plotted versus voltage in Figure 3e (right y-axis). None of the spectra show a peak shift, indicating that there is no significant halide segregation.[57] For most of the devices, the PLQY increases sharply for $V >$ maximum power point (MPP), indicative of increasing charge accumulation in the perovskite layer, while it is almost voltage-independent for $V <$ MPP, attributed to charge extraction to contact layers. As we will show via simulation results presented later, the shape of the voltage-dependent PLQY can only be properly explained once the effects of field screening by mobile ions are accounted for. To investigate
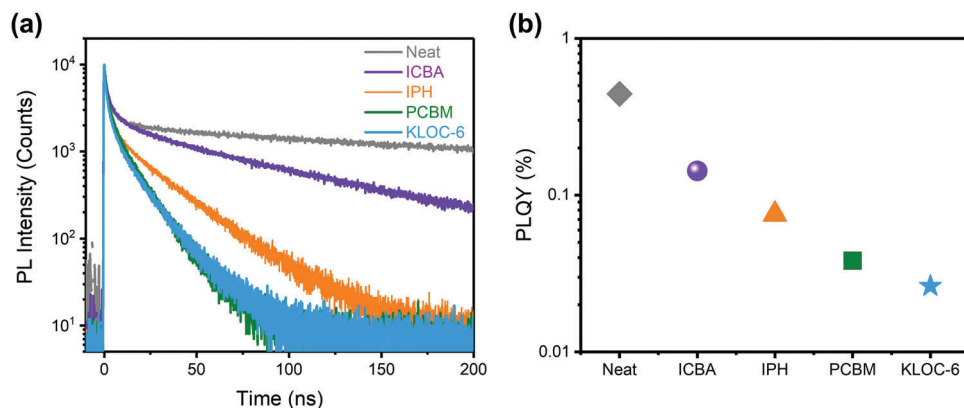
Figure 2. a) TRPL decay kinetics and b) steady-state PLQY measurement of neat perovskite films on glass with or without ETMs. In the TRPL measurements, a 405 nm pulsed laser with a fluence of 0.4 nJ cm^{-2} per pulse and a repetition frequency of 1 MHz was used for excitation, and the decay kinetics were probed at the PL peak wavelength of 790 nm. In the PLQY measurements, 532 nm CW laser with 1-sun equivalent illumination intensity was used for excitation.

Table 2. Summary of device operando PLQY results, including J–V parameters and the QFLS under both OC and SC conditions.

ETM	V_{OC} [V]	QFLS$_{OC}$ [eV]	QFLS$_{OC}$ -qV_{OC} [meV]	J_{SC} [mA cm^{-2}]	QFLS$_{SC}$ [eV]	ΔQFLS$_{OC-SC}$ [meV]
ICBA	1.10	1.12	20	17.2	1.09	30
IPH	1.10	1.11	15	22.9	1.06	50
PCBM	1.08	1.09	10	23.9	1.04	50
KLOC-6	0.99	1.06	75	21.2	1.05	10
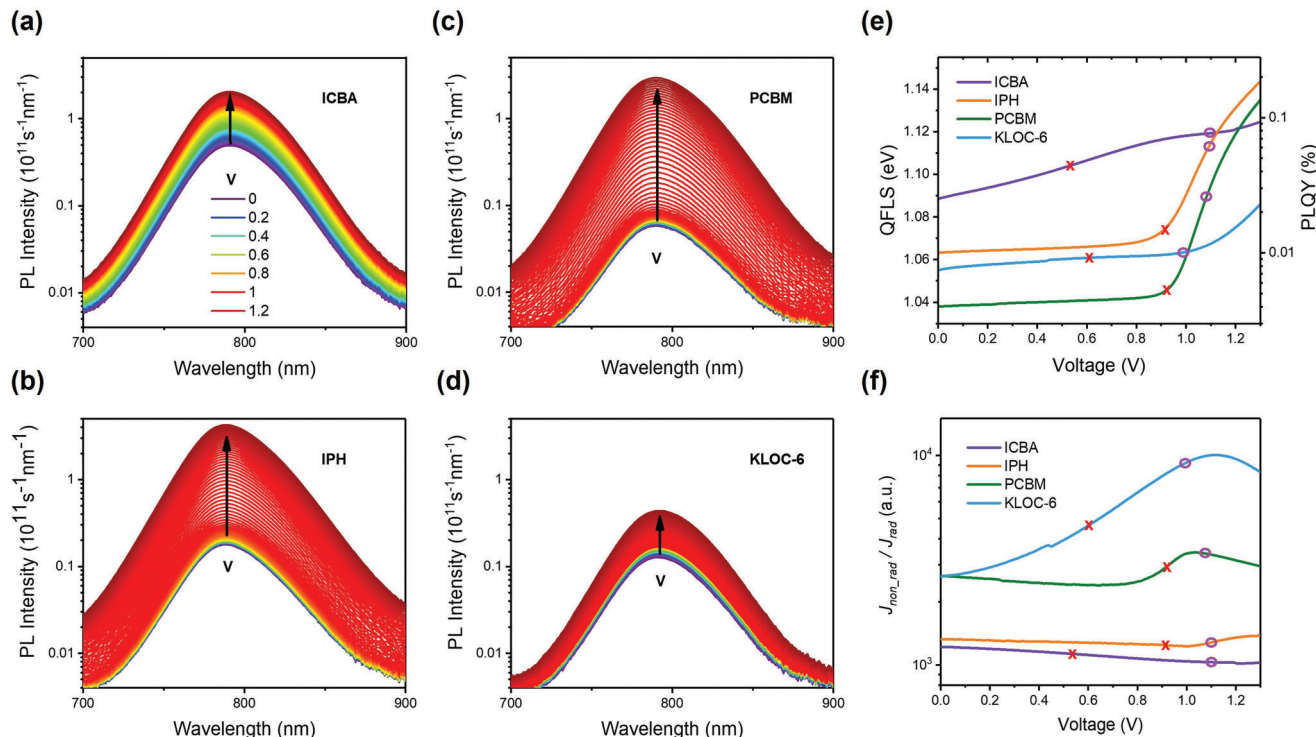
Figure 3. a–d) Operando PL spectra of a) ICBA, b) IPH, c) PCBM, and d) KLOC-6 based PSCs. The voltage increases from 0 to 1.3 V, as is indicated by the color change from blue to red, and the corresponding legend is shown in (a). e) PLQY, QFLS, and f) J_{non_rad} / J_{rad} of all devices Measurements were carried out under 1-sun equivalent 532 nm CW laser illumination, and all devices were illuminated under these conditions for 5 min prior to measurement. The values at V_{OC} and MPP for each device are marked as circles and crosses in (e) and (f), respectively.

Figure 4. Light intensity-dependent PL measurement of PSCs at OC and SC. a) Calculated QFLS and $\Delta QFLS_{OC-SC}$ of those devices with different ETMs. The solid and dashed lines are the results of fits to the equation $QFLS = QFLS_0 + b\ln(I_{exc} + a)$ for OC and SC, respectively, where $QFLS_0$ is the background QFLS, I_{exc} is 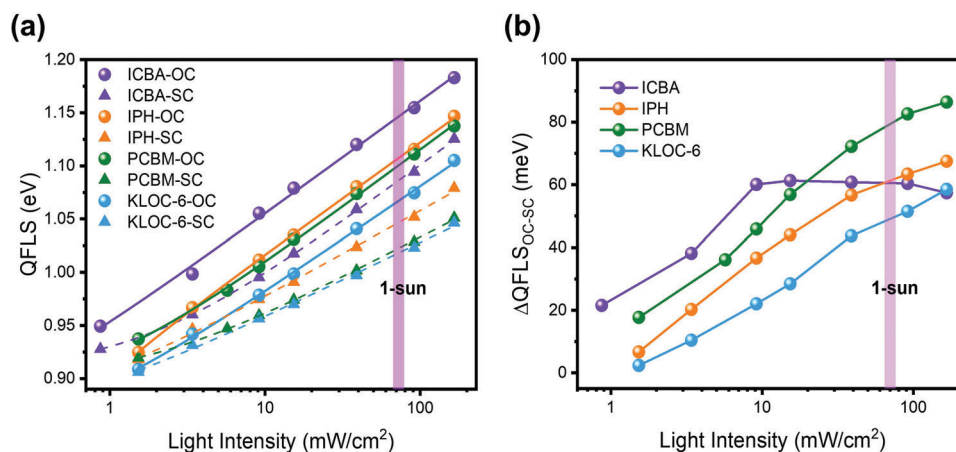the excitation fluence, a is a factor for correcting light intensity, b is the fitting parameter. No pre-illumination was applied, and the laser was blocked immediately after each measurement. The pink stripe indicates the excitation fluence equivalent to 1-sun illumination.

how the competition between the radiative and non-radiative recombination currents varies with applied voltage, we plot the ratio of the non-radiative recombination current (J_{non_rad}) to J_{rad} in Figure 3f, the latter of which includes contributions from both PL and the recombination of injected carriers (i.e., electroluminescence). We will discuss this plot further in Section 3.2.

The PLQY data were used to calculate the QFLS in each device as a function of voltage, as shown in Figure 3e (left y-axis), with the calculation details described in the Supplementary Notes to Figure S1, Supporting Information. We first consider the QFLS at V_{OC} ($QFLS_{OC}$). The KLOC-6 device has by far the lowest $QFLS_{OC}$, followed by the PCBM device, and finally the IPH and ICBA devices. This trend is consistent with the steady-state bilayer PLQY results. Next, we compare $QFLS_{OC}$ to the device qV_{OC} values, as summarized in columns 2–4 of Table 2. As expected, $QFLS_{OC}$ shows the same trend as qV_{OC}, namely ICBA ≥ IPH> PCBM> KLOC-6. However, it is striking that the difference between $QFLS_{OC}$ and qV_{OC} is significantly higher (75 meV) for the KLOC-6 device compared to the ICBA, IPH and PCBM devices (20–30 meV).

We now consider the SC QFLS ($QFLS_{SC}$) of these devices and the QFLS reduction from OC to SC ($\Delta QFLS_{OC-SC}$), as summarized in columns 6 and 7 of Table 2. Surprisingly, all the devices show high values of $QFLS_{SC}$ (>1 eV), regardless of the ETM LUMO level and mobility, indicating that there is significant electronic charge accumulation in the perovskite layer, even under SC conditions. As a result, small values of $\Delta QFLS_{OC-SC}$ are observed, with all the devices having a value ≤ 50 meV. We note these large $QFLS_{SC}$'s were measured on devices which had been exposed to 1-sun equivalent laser illumination for five minutes prior to measurement, while being held at a bias voltage near SC. Smaller $QFLS_{SC}$, and thus larger $\Delta QFLS_{OC-SC}$ (e.g., $QFLS_{SC} = 1.02$ eV and $\Delta QFLS_{OC-SC} = 80$ meV for PCBM device at 1-sun), are observed in light intensity-dependent OC and SC PL measurements without pre-illumination, as shown in **Figure 4** (full experimental details are provided in the Methods). This is consistent with previous reports that the PL of PSCs will increase following continuous il-

lumination, attributed to the effects of ion migration on both the electronic charge carrier distribution and recombination in perovskite devices.[20,58,59] However, we stress here that these "light-soaking" effects take place over longer timescales than those of the ionic motion associated with J–V hysteresis, with the former taking several minutes while the latter occur over a timescale of seconds. The simulation results presented in Section 2.7 only include the effects of ions which are mobile over the timescale of a J–V scan and do not attempt to account for the effects of light-soaking on device performance.

Having commented on the high $QFLS_{SC}$ observed in all four devices, we now consider the trend in this value between the devices. It is apparent that the PCBM device has the lowest $QFLS_{SC}$, largest $\Delta QFLS_{OC-SC}$, and highest J_{SC}, followed by IPH and then ICBA. This result implies that there is a correlation between a deeper ETM LUMO and improved electronic carrier extraction at short circuit. However, the device using KLOC-6 is an exception to this trend since, although KLOC-6 has the deepest ETM, it does not have the lowest $QFLS_{SC}$ or highest J_{SC}. In fact, it is outperformed by the PCBM device in both these figures of merit for short circuit electronic charge extraction, the reason for which will be discussed in Section 3.1.

Lastly, we also measured the devices' electroluminescence quantum efficiency (EQE_{EL}) and the results are shown and discussed more fully in Figure S6, Supporting Information and its supplementary note. We found that that the PCBM and IPH devices have the highest EQE_{EL}, perhaps due to their good energetic alignment with the perovskite conduction band, while the ICBA device shows an unexpectedly low value, which we attribute to the electron injection barrier from the Au cathode to the ETM. As expected, the KLOC-6 device has the lowest EQE_{EL}, consistent with TRPL, PLQY, and full device measurements. As will be discussed more fully in Section 3.2, we attribute these observations to the large injection barrier from the KLOC-6 to the perovskite layer, leading to electronic charge accumulation in the ETM and thus a high rate of non-radiative surface recombination.

**ADVANCED
SCIENCE NEWS**

www.advancedsciencenews.com

**ADVANCED
ENERGY
MATERIALS**

www.advenergymat.de

2.6. Light Intensity-Dependent Device PL and QFLS

In order to probe the illumination intensity dependence of the devices' performance, we performed light intensity-dependent PL measurements on the same devices under both OC and SC conditions. As described above, these measurements were conducted without pre-illumination. Compared to the operando PL, they probe the radiative recombination process without the effects of light soaking. The corresponding QFLSs were calculated via Equation (1) and the results are shown in Figure 4. In general, the QFLS increases with light intensity since a higher incident photon flux leads to a greater density of photogenerated charges. For any given incident light intensity, the $QFLS_{OC}$ values follow the same trend as was observed under 1-sun conditions in the operando PL measurement (i.e., ICBA>IPH>PCBM>KLOC-6) and are higher than the corresponding $QFLS_{SC}$ values, as is expected due to electronic charge extraction to the external circuit at SC. Surprisingly, the $QFLS_{SC}$ values also follow this trend, which is counter to the quasi-steady-state operando PL results where the KLOC-6 had a larger $QFLS_{SC}$ than the PCBM. This demonstrates the importance of stating how devices have been pre-illuminated and pre-biased when reporting the results of PL measurements so that reliable comparisons can be made between literature values.

Figure 4b compares the $\Delta QFLS_{OC-SC}$, a parameter indicative of the reduction in electronic charge carrier density in the perovskite layer between OC and SC, between the four devices. In the IPH, PCBM, and KLOC-6 devices, $\Delta QFLS_{OC-SC}$ increases with light intensity, while for ICBA it is intensity independent for excitation fluences greater than 0.1-sun equivalent. As the difference in gradient between OC and SC conditions (which is what causes the increase in $\Delta QFLS_{OC-SC}$ with intensity) is due to electronic charge extraction to the external circuit at SC, the observation of no increase in $\Delta QFLS_{OC-SC}$ for ICBA at higher light intensities indicates that the presence of electronic charge extraction does not significantly affect the dominant recombination pathways in the device once a sufficiently high carrier population is reached (the low light intensity dependence may be due to the effects of trap filling). Thus, in ICBA, most of the photogenerated electronic charges accumulate in the perovskite layer at SC and create conditions in the device which are similar to those at OC.

2.7. Device Simulations

In order to better understand the causes of electronic charge accumulation (high QFLS) near SC, we performed drift-diffusion simulations using Driftfusion, a software package which accounts for the effects of mobile ionic defects on the behavior of PSCs.[60] Details of the simulation protocol and assumptions regarding the nature of the mobile ions are given in the Supporting Information. The simulation's parameters are given in Tables S2–S4, Supporting Information and were chosen to model the performance of the PCBM device. However, we wish to stress that the aim in this section is not to accurately recreate the measured device but instead to gain a deeper insight into the effect of mobile ions upon QFLS. We also investigate the impact of ETM mobility and LUMO level on QFLS. To do this, we started from the ETM parameters given in Table S4, Supporting Information

and performed additional simulations where the parameter of interest was swept through a range of values, while other device properties were held constant. This methodology allowed us to separately evaluate the impacts of mobile ions, ETM mobility and ETM energetics on device performance.

To illustrate the role played by mobile ions in charge accumulation under SC conditions, we consider simulated J–V and QFLS-V scans, which are shown in **Figures 5**a,b and summarized in **Table 3**. By contrasting the results obtained with and without the inclusion of mobile ions, it is clear that the simulation can only reproduce the high $QFLS_{SC}$ measured by operando-PL when mobile ions are included. As shown in Figure 5c, a mobile ion density $\gtrsim 5 \times 10^{16}$ cm^{-3} is necessary to observe a significant increase in the $PLQY_{SC}$. We note that the exact value of this threshold is dependent upon other properties of the perovskite layer, such as the carriers' mobilities and bulk recombination lifetimes. By contrast, the choice of ETM mobility and LUMO has a less significant impact on the value of $QFLS_{SC}$, as is shown in Figure S7, Supporting Information. Additionally, we note that the shape of the QFLS versus voltage curve could only be accurately reproduced when mobile ions were included in the simulations. Without mobile ions, the QFLS is observed to decrease for voltages $V > V_{OC}$, the reasons for which are discussed in greater detail in the Supplementary Notes for Figure S7, Supporting Information.

To understand the difference in behavior with and without mobile ions under low voltage conditions, it is necessary to consider how electronic charge extraction is affected by the redistribution of ions in response to the electric field within the device. At (quasi) steady-state and for a sufficiently high ion density, the mobile ions will redistribute to screen the electric field in most of the perovskite layer (Figures 5e,f).[15,61,62] This means that photogenerated electronic charges must diffuse, rather than drift, to the interfaces to be extracted as current.[22] The effect of ionic shielding is most pronounced at SC, where the screening of the electric field in the perovskite bulk leads to electronic charge accumulation in the device, as demonstrated by the high $QFLS_{SC}$ values reported herein. Consequently, there is a reduction in J_{SC}, since a greater fraction of the photogenerated electronic charges recombine before they can be extracted from the device as current.[63] This electronic charge accumulation occurs even in the case of the simulated PCBM device (see Figure 5d), which has a good energetic alignment between the ETM's LUMO and the perovskite's conduction band, as well as the highest electronic carrier mobility. Despite these beneficial contact layer properties, we still find that the inclusion of mobile ions and the resultant field screening leads to a decrease in J_{SC} by 2.0 mA cm^{-2} and an increase in $QFLS_{SC}$ by 120 meV.

J_{SC} loss when ionic effects are included is due to an increase in both bulk and surface recombination at SC (Figure S8, Supporting Information), which is driven by the increased electronic carrier density in the perovskite layer (illustrated in Figure 5d). There is an increase in the SC steady-state electronic carrier density when extraction is driven by a diffusive process, rather than drift, due to the increase in the transit time of photogenerated electronic charges prior to extraction to the external circuit. To illustrate this point, we can contrast the average electronic carrier velocity at SC in the cases with and without mobile ions, which are 4.6×10^3 and 5.1×10^4 cm s^{-1} respectively (full calculation
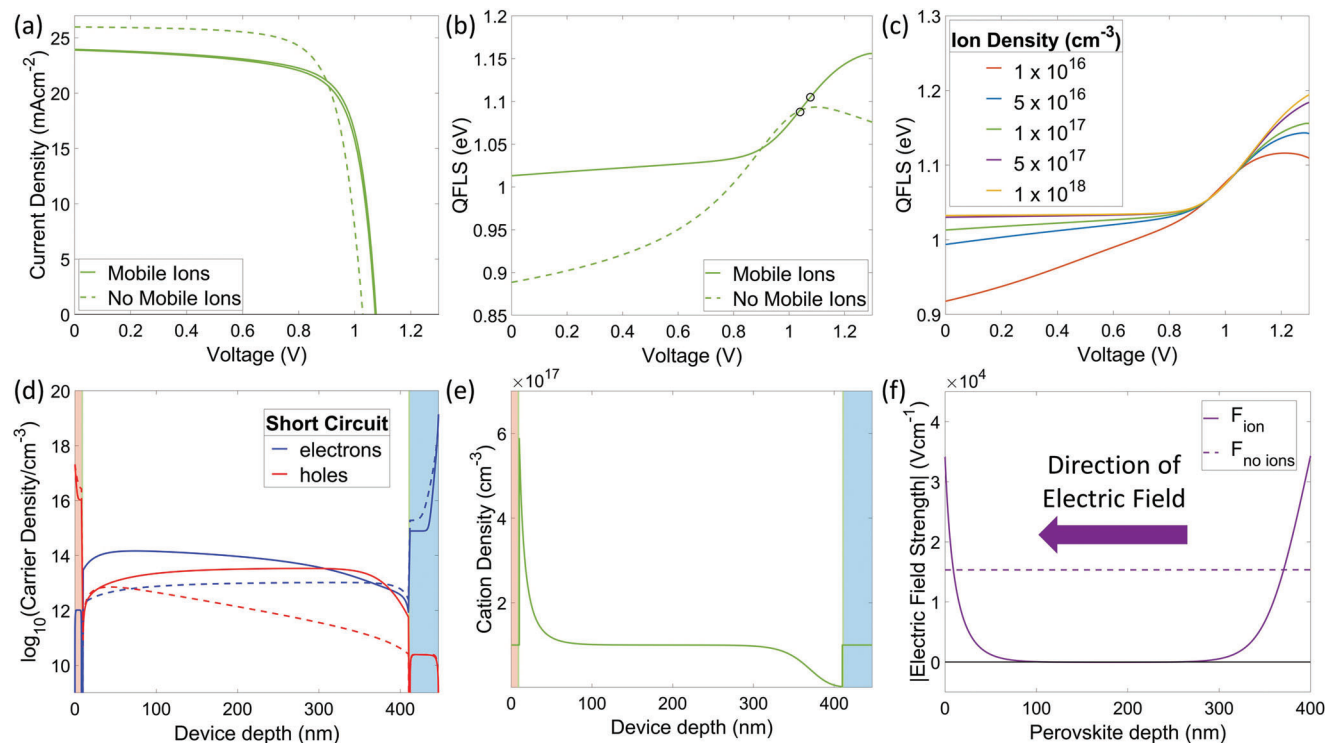
Figure 5. a) Simulated J–V curves with (solid lines) and without (dotted lines) the inclusion of mobile ions. The J–V parameters are summarized in Table S5, Supporting Information. J–V scans were simulated under continuous-wave 532 nm laser illumination and using a scan rate of 10 mV s^{-1}, comparable to the rate of 7 mV s^{-1} used in the operando PL measurements. b) Simulated QFLS versus voltage scans with (solid lines) and without (dotted lines) the inclusion of mobile ions. The black circles indicate the QFLS at OC. It is apparent that the high value of PLQY at SC measured via operando PL can only be recreated when mobile ions are included in the simulation. Additionally, the QFLS is observed to decrease at high voltages in the case with no mobile ions, which is contrary to the experimental results. c) The QFLS versus voltage as the density of mobile ions is varied. For the perovskite parameters used here, a mobile ionic density > 5 × 10^{16} cm^{-3} is needed to see a significant increase in QFLS$_{SC}$. d) Charge carrier distributions at SC with (solid lines) and without (dashed lines) mobile ions. The inclusion of mobile ions leads to higher carrier concentrations at SC and a more uniform carrier distribution, which is due to the screening of the built-in field. e) Ionic distribution under SC conditions. The ions have redistributed in response to the built-in field of the device, meaning that cations have accumulated at the hole transport material/perovskite interface. f) The electric field (F) in the perovskite layer under SC conditions with (solid lines) and without (dotted lines) the inclusion of mobile ions. In the case without mobile ions, the built-in field is distributed uniformly across the perovskite layer, driving efficient charge extraction at SC. By contrast, in the case with mobile ions, the electric field is restricted to narrow accumulation and depletion regions at the interfaces between the perovskite and the transport materials, creating a field-free region in the perovskite bulk.

details and assumptions are given in the Supporting Information), demonstrating that there is an order of magnitude difference in the average velocities of diffusion and drift-driven electronic carriers. As electronic carriers spend longer in the device in the diffusion-driven regime, they are more likely to undergo recombination, a fact which has already been recognized in the manufacture of mature technologies, such as silicon solar cells, in which thicknesses of the emitter and base layers are optimized so that electronic carriers are produced within a diffusion length of either the device's n-p junction or its electrodes.[64] Additionally, the necessity of a built-in field to aid electronic charge extraction has been recognized in the design of amorphous silicon (α-Si) solar cells, which commonly use a p-i-n structure to overcome the short diffusion lengths inherent to this material.[65]

Lastly, we consider Figure S7, Supporting Information to elucidate the relationships between ETM properties and device performance. These figures show the QFLS versus voltage as the ETM mobility (Figure S7a, Supporting Information) and ETM LUMO level (Figure S7b, Supporting Information) are varied through

Table 3. Summary of the simulated J–V and PL–V scans for the baseline PCBM device with and without the inclusion mobile ions in the simulation. The presence of mobile ions leads to a reduction in ΔQFLS$_{OC\text{-}SC}$, which is due to the increase in QFLS$_{SC}$ when the effects of ionic field screening at SC are accounted for.

	V_{OC} [V]	QFLS$_{OC}$ [eV]	QFLS$_{OC}$ – qV_{OC} [meV]	J_{SC} [mA cm^{-2}]	QFLS$_{SC}$ [eV]	ΔQFLS$_{OC\text{-}SC}$ [meV]
Mobile ions	1.08	1.10	20	24.0	1.01	90
No mobile ions	1.03	1.09	60	26.0	0.89	200

the ranges 10^{-3}–10^{-5} cm^2 V^{-1} s^{-1} and 3.75–4.15 eV, respectively, and all other simulation parameters are held constant. In general, we observe that a decrease in the ETM mobility reduces ΔQFLS$_{OC\text{-}SC}$ due to a higher QFLS$_{SC}$, with QFLS$_{OC}$ being almost unchanged. The increase in QFLS$_{SC}$ as ETM mobility decreases is due to slower carrier transport through the ETM, which reduces the rate at which carriers are extracted from the bulk and leads

to greater electronic charge accumulation at the perovskite/ETM interface (see Figure S9, Supporting Information). These results suggest that the low mobility of KLOC-6 is responsible for its unexpectedly large $QFLS_{SC}$ and agree with literature reports that organic contact layers can be the limiting factor on electronic carrier transport through p-i-n PSCs.[66,67] However, we note that the ETM mobility has to be decreased by two orders of magnitude for the effect on $QFLS_{SC}$ to become significant, suggesting that the increase in $QFLS_{SC}$ seen for ICBA is due to the combination of its relatively low mobility and its poor energetic alignment with the perovskite conduction band rather than its mobility alone, which is comparable to that of IPH. To confirm this, we now consider the effects of the ETM LUMO level on QFLS (Figure S7b, Supporting Information). The results demonstrate that, when the perovskite conduction band lies below the ETM LUMO (as is the case for ICBA) there is an increase in $QFLS_{SC}$ since the energetic barrier to electron extraction causes electron accumulation in the bulk. Additionally, under OC conditions, the simulations reproduce the experimental trend that a shallower ETM LUMO level correlates with a higher $QFLS_{OC}$.

3. Discussion

3.1. Electronic Carrier Transfer and Extraction

By combining our operando PL measurements with simulations, we have demonstrated that the presence of mobile ions in the perovskite active layer reduces the efficiency of electronic carrier extraction in PSCs. Under SC conditions, mobile ions redistribute to screen the device's built-in field and thus electronic carrier transport is driven by diffusion, rather than drift. Our simulations indicate that this mechanism is present in all devices, regardless of transport material properties such as mobility and energetics, and typically leads to an increase in $QFLS_{SC}$ by ≈100 meV (see Figure 5b and Figure S7, Supporting Information). The effect of mobile ions on electronic carrier extraction is also apparent from the small values of $\Delta QFLS_{OC-SC}$ (≤ 50 meV) which were measured in operando PL. Considering our best best-performing PCBM based PSC (PCE of ≈20%), the measured value of $\Delta QFLS_{OC-SC}$ corresponds to a reduction in the perovskite's electronic charge carrier density by a factor of between 3 and 7, with the precise value depending on the degree of imbalance between the electron and hole populations in the perovskite (calculation discussed further in the Supporting Information). This value is especially striking when compared to that measured in many other solar cell technologies, such as GaAs, Cu(In,Ga)Se$_2$, dye-sensitized solar cells (DSSCs) and organic solar cells (OPVs), which have reported OC to SC charge density reductions of over one order of magnitude.[68–72] Finally, to further quantify the effect of mobile ions on electronic carrier extraction at short circuit, we calculated the generation current, J_{gen}, in these devices using the method illustrated in Figure S10, Supporting Information. This allows us to estimate the decrease in J_{sc} due to mobile ions by performing the calculation $J_{loss} = J_{gen} - J_{SC}$. This gives a value of over 2 mA cm^{-2} for the PCBM device, highlighting the impact of field screening by the redistribution of mobile ions on electronic charge extraction efficiency.

In addition to this baseline reduction in the extraction efficiency of electronic carriers due to the presence of mobile ions, our results also allow us to investigate the effect of ETM energetics and mobility on electronic carrier transfer and extraction. We note that, as all the ETMs considered in this study were undoped, we focus upon their mobility as a figure of merit for electronic carrier transport, as this will be the factor which determines their relative conductivities. The results of our TRPL and TAS measurements, presented in Section 2.4, provide strong evidence that deepening the LUMO of the ETM improves the efficiency of electronic charge transfer from the perovskite to the ETM. However, as these are transient measurements, they cannot tell us about the efficiency of electronic charge extraction under the steady-state conditions which are relevant in a device at short circuit. For this, we instead turn to the results of our operando PL and intensity dependent QFLS measurements (Sections 2.5 and 2.6, respectively).

In the cases of ICBA, IPH, and PCBM, our operando-PL results demonstrate a correlation between a shallower ETM LUMO and less efficient electronic carrier extraction, with the $QFLS_{SC}$ being 50 meV larger in the ICBA device than the PCBM device. Indeed, the poor extraction properties of ICBA are also highlighted in our intensity dependent QFLS measurements, in which we observed a plateau in $\Delta QFLS_{OC-SC}$ for this device, indicating a negligible change in the device's dominant recombination pathways between OC and SC conditions and thus significant electronic carrier accumulation at SC.

However, as commented on in Section 2.5, the KLOC-6 device is an exception to this trend between ETM energetics and electronic charge extraction efficiency due to its combination of a deep LUMO with an anomalously low J_{SC} and high $QFLS_{SC}$. Our simulation results demonstrate that this can be attributed to the low mobility of KLOC-6 (one order of magnitude lower than that of PCBM as measured in the SCLC and TFT measurements presented in Figures S2 and S3, Supporting Information). As is shown in Figure S9, Supporting Information, reducing the ETM mobility leads to an accumulation of electrons at the perovskite/ETM interface under SC conditions, increasing the average electronic carrier density in the perovskite layer and thus enhancing the $QFLS_{SC}$ and leading to additional recombination losses under SC conditions.

3.2. Non-Radiative Recombination Losses

Our PLQY measurements on perovskite/ETM bilayers and our operando-PL measurements both show that there is a correlation between a shallower ETM LUMO and a higher $QFLS_{OC}$, which mirrors the observed increase in device V_{OC} (compare columns 2 and 3 of Table 2). Additionally, the KLOC-6 device, which has the deepest ETM LUMO, suffers from the largest discrepancy between $QFLS_{OC}$ and V_{OC} (75 meV). Given that a free energy loss between the QFLS and externally measured qV_{OC} can result from surface recombination losses at both the PTAA/perovskite and perovskite/ETM interfaces[11] and that the PTAA/perovskite interface remains the same in all four devices, the large $QFLS_{OC} - qV_{OC}$ loss observed in the KLOC-6 device is clearly indicative of enhanced surface recombination at the perovskite/ETM interface relative to the other devices. This
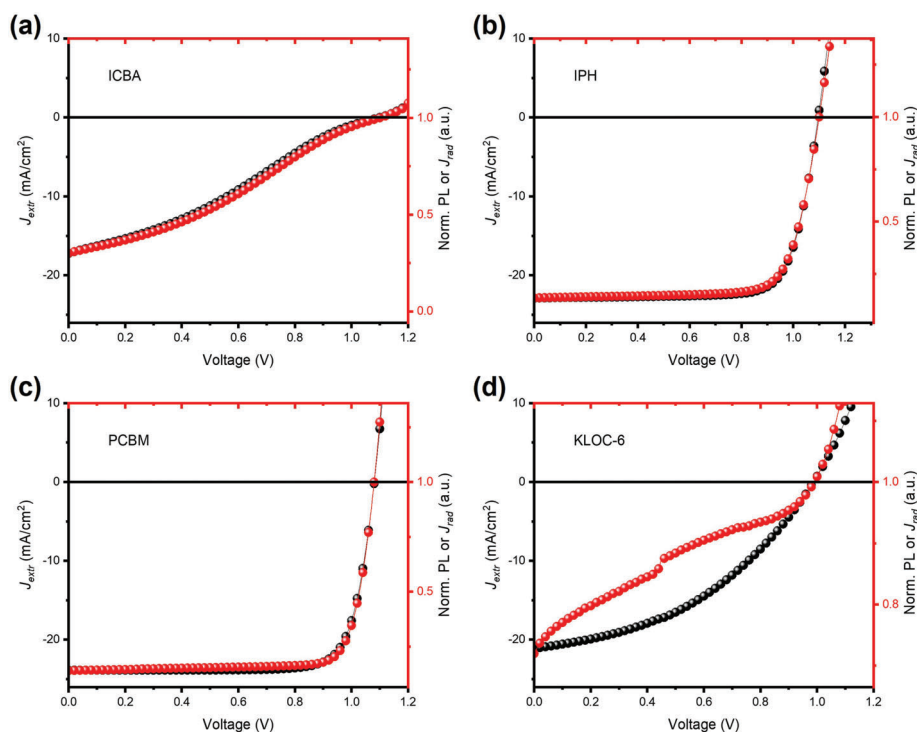
Figure 6. The PL or radiative current (red) compared with the extracted current (black) by matching their 0 V and V_{OC} points. Each PL or radiative current curve is normalized to its value at open circuit. All curves originate from the operando PL data in Figure 3 and Figure S13, Supporting Information.

conclusion is supported by the simulation results shown in Figure S11, Supporting Information, which demonstrate that a deeper ETM LUMO leads to a greater fraction of the recombination occurring at the perovskite/ETM interface. We note that replicating this effect in the simulations required no change in the surface recombination velocity at the perovskite/ETM interface, suggesting that the enhanced recombination in the KLOC-6 device can be largely explained by the ETM energetics, rather than a difference in the quality of the perovskite/ETM interface. Instead, we attribute the increase in surface recombination to greater electron accumulation in the KLOC-6 due to its deep LUMO level. Since the LUMO of KLOC-6 lies below the perovskite conduction band, there will only be a small energetic offset between the LUMO of KLOC-6 and the electron quasi-Fermi level for voltages above MPP. Thus, there will be a higher density of electrons in the KLOC-6 than is present in the other ETMs, which have shallower LUMOs, and these electrons in the KLOC-6 act as a reservoir of charge to undergo surface recombination with perovskite holes, which accelerates surface recombination.[73]

The presence of an additional recombination mechanism in the KLOC-6 device is further illustrated in **Figure 6**a–d, in which we make a direct comparison between the operando J–V and PL–V data by matching the two curves to their values at 0 V and V_{OC}. Whilst absolute current density is used for the J–V curve, the PL or J_{rad} are normalised to the value at V_{OC} due to there being no net charge extraction or injection at this critical point. Therefore, these plots allow us to compare the voltage-dependence of a device's radiative loss current (J_{rad}) to that of its extracted current (J_{extr}).[4,40,56] As $J_{extr} = J_{gen} - J_{rad} - J_{non\_rad}$ and

$J_{non\_rad} \gg J_{rad}$ for these devices (see Figure 3f), we can write that $J_{extr} \approx J_{gen} - J_{non\_rad}$. Thus, the voltage dependence of J_{extr} is determined by the voltage dependence of J_{non_rad}. This means that a discrepancy in the shapes of the PL–V and J–V curves will occur when the radiative and non-radiative loss currents have different dependencies on the applied voltage (i.e., different ideality factors).

It is evident that in Figure 6 the PL–V and J–V curves in the range of 0 V – V_{OC} show minor discrepancy for the devices with ICBA, IPH, and PCBM, whereas the curves for KLOC-6 based devices diverge noticeably. We note here that the minor discrepancy observed in the ICBA, IPH, and PCBM devices is surprising, given that one might expect the radiative and non-radiative loss currents to have different dependencies on applied voltage. However, a full understanding of the reasons for this lie beyond the scope of this work and we instead focus on the large discrepancy in the curves which is observed for the KLOC-6 device. Considering the discussion above and the larger value of $QFLS_{OC} - qV_{oc}$ measured for KLOC-6, we propose that the large discrepancy between this device's PL–V and J–V provide further evidence that there are greater surface recombination losses at the perovskite/KLOC-6 interface than at the other perovskite/ETM interfaces.

Moreover, comparisons between forward and reverse scans of the J–V and PL–V are shown in Figure S12, Supporting Information, with negligible hysteresis in PCBM, minor in ICBA and IPH, and severe in KLOC-6. This trend agrees with that predicted in the literature, namely that the severity of J–V hysteresis increases with impeded charge extraction,[74] or increased rates of interfacial recombination.[16] Thus, these results provide

additional evidence that the KLOC-6 device has a higher rate of non-radiative surface recombination at the perovskite/ETM interface and that the impact of this recombination pathway can be reduced by using an ETM with a shallower LUMO, as is demonstrated by the PCBM, IPH, and ICBA devices.

We now discuss Figure 3f, which shows the ratio between the devices' non-radiative and radiative recombination currents (J_{non_rad}/J_{rad}). We can calculate the radiative recombination current (J_{rad}) directly from $e\varphi$, where e is the electron charge, φ is the measured absolute emission flux. However, the non-radiative recombination current (J_{non_rad}) cannot be accessed directly and is instead determined via $J_{gen} - J_{rad} - J_{extr}$, where J_{gen} is the generation current and J_{extr} is the extraction current. Figure S13 summarizes all the recombination currents and describes the details of the calculation in its Supplementary Notes. Although there is some uncertainty in the value of J_{gen}, we note that the conclusions drawn from the ratio J_{non_rad}/J_{rad} in this section are not sensitive to its absolute value, as illustrated in Figure S14, Supporting Information.

Considering the magnitudes of the ratios shown in Figure 3f, we note that J_{non_rad} is at least 1000× larger than J_{rad} for all the devices, across the entire voltage range. This demonstrates the dominance of non-radiative recombination pathways in these devices and the potential for further improvements in V_{OC}. Additionally, we see that J_{non_rad}/J_{rad} is significantly larger for KLOC-6 than for the other devices at $V > $ MPP, emphasising the higher rate of non-radiative recombination in this device. As discussed above, this is due to the higher rate of surface recombination at the perovskite/ETM interface in the KLOC-6 device. Surprisingly, given the close match between the J–V and PL–V curves commented upon in Figure 6, we see a similar, though less severe, increase in J_{non_rad}/J_{rad} for PCBM in the voltage range 0.8 V–V_{OC}. This indicates that surface recombination at the perovskite/ETM interface becomes a more significant loss mechanism in the PCBM device at higher voltages (i.e., higher carrier densities), though not to such an extent that it causes obvious discrepancy between the values of QFLS$_{OC}$ and qV_{OC}. Thus, this figure further demonstrates that an ETM LUMO which lies below the perovskite conduction band is correlated with a higher rates of surface recombination at the perovskite/ETM interface. As stated previously, to explain this observation we propose that the rate of surface recombination at the perovskite/ETM interface depends upon both the hole population in the perovskite layer and the electron population on the undoped ETM, which will increase rapidly as the electron quasi-Fermi level approaches the ETM's LUMO.[25,46] .This indicates that minimizing charge accumulation on transport layers could be key to further improving p-i-n devices and may help to rationalize the improvement in V_{OC} which is seen upon switching from PTAA to ultrathin self-assembling monolayers such as 2PaCz. Not only are these monolayers reported to have deeper highest occupied molecular orbitals than PTAA, improving their energetic match with the perovskite valence band, but they are also unlikely to act as reservoirs of holes for recombination due to them consisting of only a single layer of molecules.[75–78]

4. Conclusion

In summary, we have used operando PL spectroscopy as a tool to quantify the radiative and non-radiative recombination in four p-i-n PSCs under operating conditions. We observed a large (>1 eV) QFLS in all our devices under short circuit conditions, regardless of ETM properties and overall device performance. By drawing upon the results of Driftfusion simulations, we can conclude that this effect is an additional consequence of ion migration in the perovskite layer, which occurs because, at low applied voltages, mobile ions located at the perovskite/contact layer interfaces screen the internal electric field, impeding electronic charge extraction, and reducing J_{SC}. Additionally, our intensity dependent device PL measurements suggest this effect may be further enhanced by light soaking.

Our results also provide mechanistic insight into the link between energetic alignment at the perovskite/ETM interface and device performance. Whilst a deep LUMO favors electronic charge transfer from the perovskite to the ETM, it can result in increased non-radiative recombination at the perovskite/ETM interface, which limits the PSC's V_{OC}. On the contrary, although a shallow LUMO benefits the QFLS in the bulk perovskite, it impedes electronic charge extraction under low voltage conditions (when $V < V_{OC}$), leading to the accumulation of photogenerated electronic charges in the perovskite layer. This results in a device with a low J_{SC} and/or FF. Moreover, by analyzing the ratio of non-radiative to radiative recombination currents as a function of applied voltage, we found evidence that surface recombination at the perovskite/ETM interface is more severe at voltages close to V_{OC} than it is under low-voltage conditions. However, it is only the dominant recombination process in devices which use ETMs whose LUMO lies beneath the perovskite's conduction band. This can be attributed to the formation of a non-ohmic contact at the ETM/perovskite interface, causing electrons to accumulate in the ETM at high voltages. Thus, our work gives greater insight into the reasons why the energetic alignment at the perovskite/ETM interface has such a significant impact on device performance and demonstrates the consequence of field screening caused by ion migration in the perovskite layer both experimentally and using simulations.

5. Experimental Section

Perovskite Precursor Solution Preparation: 1.25 M FA$_{0.95}$Cs$_{0.05}$PbI$_{2.8}$Br$_{0.2}$ was prepared by dissolving formamidinium iodide (FAI, 99.99% purity, Great Cell Solar), cesium iodide (CsI, 99.9% purity, AlfaAesar), lead iodide (PbI$_2$, 99.99% purity, TCI), and lead bromide (PbBr$_2$, 99.99% purity, TCI) at a molar ratio of 0.95:0.05:0.9:0.1 in anhydrous *N,N*-Dimethylmethanamide (DMF, Sigma) / *N*-Methyl-2-pyrrolidone (NMP, Sigma) (4:1 volume ratio).

Perovskite Solar Cell Fabrication: ITO was sequentially cleaned in acetone, detergent solution (Decon 90), deionized water, acetone, and isopropanol for 5 minutes in each solvent. The ITO was then dried with nitrogen and treated by oxygen plasma for 8 min. PTAA (Ossila 14 000 mW, 2.5 mg mL^{-1} in toluene) was then spin-coated on the ITO at 3000 RPM with an acceleration of 5000 RPM for 20 s. To improve the wetting property, PFN-Br (1-Material, 0.05 wt% in methanol) was then spin-coated on top of the PTAA at 5000 rpm with an acceleration of 5000 rpm for 20 s. The substrates were then transferred into a nitrogen-filled glove box afterward. The perovskite precursor was spin-coated on the as-prepared substrates at 4000 rpm with an acceleration of 4000 rpm for 20 s, and after 10 s, 0.4 mL of diethyl ether was rapidly dropped onto the substrate. The substrate was then immediately annealed at 65 °C for 2 min before further annealing at 150 °C for 15 min. After the substrates were cooled to room temperature, the different electron transport materials (ETMs), including ICBA

(Solenne, 99%, 15 mg mL^{-1} in chlorobenzene), IPH (Solenne, 99% purity, 30 mg mL^{-1} in chlorobenzene), PCBM (Solenne, 99.5% purity, 30 mg mL^{-1} in chlorobenzene), and KLOC-6 (Solenne, 99% purity, 15 mg mL^{-1} in chlorobenzene), were then spin-coated on top of the perovskite layer at 2000 rpm with an acceleration of 4000 rpm for 20 s. The concentration of the ETM was chosen to optimize device performance. BCP (Lumtec, 99.5% purity, 0.5 mg mL^{-1} in methanol) was then spin-coated on top of the ETM at 5000 rpm with an acceleration of 5000 rpm for 20 s. Immediately after BCP was deposited, the substrates were transferred for thermal evaporation. Finally, 100 nm of Au with a pixel area of 0.09 cm^2 was thermally evaporated as a top contact at a base pressure of 5 × 10^{-6} mbar.

Operando Photoluminescence Measurement: A home-built system was coupled with an integrating sphere (AvaSphere-50-REFL, AVANTES), a spectrograph (Kymera 193i, Andor), and a CCD camera (DU420A-BEX2-DD, Andor) for the PL spectrum collection, a potentiostat (Ivium Vertex.100 mA.EIS) was used to apply a voltage and record current, and a CW 532 nm laser diode module (THORLABS, CPS532^b) was used for photoexcitation. A Labview code was specially developed for system control and data collection. A mercury light calibration source (AvaLight-CAL-MINI, AVANTES) was used to correct the spectrometer wavelength, and a halogen light source (AvaLight-HALCAL-ISP50-MINI, AVANTES) used for the absolute photon flux calibration. The laser excitation intensity was adjusted to 1-sun equivalent by matching the J_{SC} of a PCBM device under a 532 nm laser to that under a solar simulator. A mask smaller than the pixel area was used during the measurement to ensure all exposure areas were covered with electrodes. All devices were encapsulated within a sealed sample holder in the nitrogen-filled glove box prior to undertaking any measurements to avoid air exposure. The operando PL measurements were undertaken at a scan rate of 7 mV s^{-1}. Prior to measurement, the PSCs were soaked for 5 min under the laser light, while being held at a bias voltage of 0.2 V. This bias voltage was used as it is the default setting of the equipment. The devices were left for 5 minutes as it was observed that this time was sufficient for the device performance to stabilize.

Light Intensity-Dependent Photoluminescence Measurement: A calibrated PL system with the same set-up as the operando PL measurement was used. However, in this experiment, the PL emission was only measured under open circuit and short circuit conditions for each illumination intensity, rather than measuring across the *J–V*. Different excitation intensities were achieved by passing the laser through a selection of neutral density filters and the measurements were taken by moving sequentially from the lowest intensity to the highest intensity. The light intensity was measured with a digital power meter (THORLABS, PM100D) and a photodiode sensor (THORLABS, S120VC). In this measurement, no pre-illumination/ light soaking procedure was conducted before measuring each of the spectra, and the laser was immediately blocked after each spectrum was collected. This ensured a total laser exposure time of <2 s, with a longer exposure used at lower intensities to ensure a good signal to noise ratio. The devices were kept in the dark for at least 30 s before collecting the next spectrum and during this time the ND filters, bias potential (i.e., open circuit or short circuit) and acquisition settings were changed as necessary. During the measurements at short circuit, the photocurrent was also recorded.

Film Photoluminescence Measurement: The steady-state film PLQY measurement was carried out using the same system and the same excitation conditions as the operando PL measurements. All samples were encapsulated under N$_2$ and were excited from the side opposite to the perovskite/ETM interface.

Photoluminescence, Electroluminescence Quantum Yield and QFLS Determination: The system was calibrated by shining a halogen lamp of known spectrum and irradiance into the integrating sphere. A spectral correction factor was determined to ensure the measured lamp spectrum matched its known spectral irradiance. The spectral intensity of the corrected spectrum was then divided by photon energy and numerically integrated to obtain the absolute photon count for the excitation, photoluminescence, and electroluminescence. The PLQY was determined by dividing the PL photon flux by the excitation photon flux while the EQE$_{EL}$ was determined by dividing the EL photon flux by the flux of injected electron-hole pairs calculated from dark current. The calculation of QFLS used Equation (1),

where J_{rad} was calculated by converting the absolute emitted photon flux into equivalent radiative currents (photons per second multiplied by elementary charge). The $J_{0, rad}$ was estimated using the same method as in previous reports[27,33] which involves multiplying the black body radiation emission spectrum with the EQE$_{PV}$ of the PCBM device, see more details in Figure S1, Supporting Information.

AM 1.5G Current–Voltage Measurement: The *J–V*s were carried out under one sun (AM 1.5) illumination from a calibrated solar simulator with a Xenon lamp (LOT) and recorded by a Keithley 2400 source meter.

Solar Cell External Quantum Efficiency Measurement: The EQE$_{PV}$ spectrum of PCBM-based PSC was conducted under a halogen lamp chopped to a frequency of 188 Hz through a Newport monochromator with a four-point probe in connection with a lock-in amplifier for data collection. A silicon photodiode was used for the reference calibration, and the data were analyzed with Tracer 3.2 software (LOT) to produce the EQE$_{PV}$ spectra.

Ultrafast Transient Absorption Spectroscopy Measurement: Ultrafast TAS measurement was carried out by using an amplified Ti:sapphire laser (Solstice, Spectra Physics), with an 800 nm laser pulse (<200 fs, 1 kHz repetition rate). The laser pulse is divided into the pump and the probe by using a beam splitter. The pump laser at the excitation wavelength (635 nm) used is generated through an optical parametric amplifier (TOPAS Prime, Light Conversion) and a frequency mixer (NirUVis, Light Conversion). The probe pulse at specific time delays is generated through a mechanical delay stage, which delay it by an adjustable period (maximum of 6 ns) relative to pump pulse. The continuous white light probe in the 450−800 nm region is generated by focusing the probe pulse into a sapphire crystal. Then, the probe pulse is divided before the sample into two pulses, one is directed to the sample and the other is used as the reference. Both pulses are directed to separated multichannel spectrometer. The continuum probe pulse on the samples is spatially overlapped with the pump pulse. The pump pulse is chopped by a synchronized chopper with a frequency of 500 Hz. Pulse energies were measured using an energy meter (OPHIR Photonics, VEGA P/N 7Z01560) with a 500 μm diameter aperture. The samples were encapsulated in a N$_2$ glove box before the measurement.

Ultraviolet–Visible Absorbance and Reflectance: The ultraviolet–visible absorbance and reflectance spectra were acquired from a Shimadzu UV-1601 spectrophotometer. The reflectance was obtained by measuring the absolute reflected light from the sample through an integrating sphere comparing to a reference light measured from a barium sulphate plate.

Time-Resolved Photoluminescence Measurement: The TRPL decays were recorded by a Delta Flex system (detector: PPD-900, Horiba scientific). A 405 nm laser diode with <200 ps pulse duration (NanoLED, Horiba scientific) was used for excitation with repetition rate of 1 MHz and fluence of 0.4 nj cm^{-2} per pulse.

Space-Charge-Limited Current Measurement: Electron only devices were fabricated onto patterned ITO-coated glass, previously cleaned in detergent and water, and then ultrasonicated in acetone and isopropyl alcohol for 15 min each. The device structure employed is ITO/ZnO/PEIE/ETM/Ca/Al. Zinc oxide (ZnO) precursor solution was prepared from zinc acetate dihydrate (219.5 mg), ethanolamine (60 μL), and 2-methoxyethanol (2 mL). This ZnO precursor solution was filtered through a 0.45 μm Acrodisc filter, spin-coated onto the plasma-treated substrates at 4000 rpm for 40 s, and annealed at 180 °C for 15 min. This process is followed by a rinsing step with PEIE (polyethyleneimine ethoxylated, 0.5% wt in 2-methoxyethanol) and further anneal at 100 °C for 10 min to dry. All ETM thin films are then deposited in inert conditions in chlorobenzene at a spin speed of 1 krpm. Calcium (Ca—20 nm) and Aluminum (Al—100 nm) were then deposited by evaporation through a shadow mask giving with pixel areas of 0.045 cm^2.

Thin-Film Transistor Measurement: Bottom contact, top gate (BC-TG) thin film transistors were fabricated in a nitrogen-filled glove box in order to evaluate the electron charge carrier mobility. Glass substrates were cleaned by sonication in a detergent solution (Decon 90), followed by sonication in acetone and isopropanol for 5 min respectively. Gold source drain electrodes of 40 nm were deposited via thermal evaporation through shadow masks (device channel length 30 um and width 1000 um) in a high vacuum (5 × 10^{-6} mbar). The ETMs were spin-coated from a

20 mg mL^{-1} solution in chlorobenzene at 1500 rpm for 30 s, followed by 10 min of thermal annealing at 100 °C. As the dielectric layer, 900 nm of CYTOP were used, and 40 nm of aluminum were thermally evaporated as the gate electrode. Electrical characterization was conducted using a Keithley 4200 SCS in a nitrogen filled glovebox.

Driftfusion Simulation: The simulations were performed using Driftfusion, which is an open-source code for simulating ordered semiconductor devices with mixed ionic-electronic conducting materials in 1D.[60] The simulation parameters used for the ETM, hole transport material, and perovskite layers are provided in the Supporting Information and were chosen to be representative of the PCBM device used in the experimental measurements. However, the authors do not assume that the simulation results are a fully accurate representation of the conditions within the PSC and instead focus their discussion on the trends which were found to be the most robust across a wide range of input parameters. A detailed description of the simulation protocols is given in the Supporting Information.

Supporting Information

Supporting Information is available from the Wiley Online Library or from the author.

Conflict of Interest

The authors declare no conflict of interest.

Author Contributions

W.X. and L.J.F.H. contributed equally to this work. W.X. fabricated the samples and devices, performed the spectroscopic experiments, and analyzed the data. L.J.F.H. carried out the Driftfusion simulation under the supervision of P.R.F.B. W.X. designed and built the operando PL system with B.M. carried out the control software development. B.M. also contributed to the operando PL data processing and analysis. P.C. contributed the method of QFLS determination and discussed the film PLQY measurement with R.D.J.O. under the supervision of H.J.S. R.D.J.O. conducted the film PLQY measurements and calculation under the supervision of H.J.S. T.J.M. optimized the recipe for solar cell fabrication and carried out the EQE$_{PV}$ measurement. N.C. supervised the SCLC measurement and discussed the results, which were measured by F.F. J.P. conducted the TFT measurements and data analysis under the supervision of M.H. R.A.P. contributed with discussion and feedback throughout this project. W.X. and L.J.F.H. wrote the manuscript. J.R.D. guided and supervised the overall project. All authors discussed the results and reviewed the manuscript.

Data Availability Statement

The data that support the findings of this study are available from the corresponding author upon reasonable request.

[1] NREL, Best Research-Cell Efficiency Chart, https://www.nrel.gov/pv/cell-efficiency.html (accessed: July **2023**).

[2] M. Kim, J. Jeong, H. Lu, T. K. Lee, F. T. Eickemeyer, Y. Liu, I. W. Choi, S. J. Choi, Y. Jo, H. B. Kim, S. I. Mo, Y. K. Kim, H. Lee, N. G. An, S. Cho, W. R. Tress, S. M. Zakeeruddin, A. Hagfeldt, J. Y. Kim, M. Grätzel, D. S. Kim, *Science* **2022**, *375*, 302.

[3] J. Leng, J. Liu, J. Zhang, S. Jin, *J. Phys. Chem. Lett.* **2016**, *7*, 5056.

[4] M. Stolterfoht, V. M. Le Corre, M. Feuerstein, P. Caprioglio, L. J. A. Koster, D. Neher, *ACS Energy Lett.* **2019**, *4*, 2887.

[5] W. Xu, T. Du, M. Sachs, T. J. Macdonald, G. Ming, L. Mohan, C.-T. Lin, J. Wu, R. Pacalaj, S. A. Haque, M. A. McLachlan, J. R. Durrant, *Cell Rep. Phys. Sci.* **2022**, *3*, 100890.

[6] R. J. E. Westbrook, T. J. Macdonald, W. Xu, L. Lanzetta, J. M. Marin-Beloqui, T. M. Clarke, S. A. Haque, *J. Am. Chem. Soc.* **2021**, *143*, 12230.

[7] M.-C. Wu, S.-H. Chan, M.-H. Jao, W.-F. Su, *Sol. Energy Mater. Sol. Cells* **2016**, *157*, 447.

[8] G. J. A. H. Wetzelaer, M. Scheepers, A. M. Sempere, C. Momblona, J. Ávila, H. J. Bolink, *Adv. Mater.* **2015**, *27*, 1837.

[9] J. Chen, N. G. Park, *Adv. Mater.* **2018**, *31*, 1803019.

[10] S. Feldmann, S. Macpherson, S. P. Senanayak, M. Abdi-Jalebi, J. P. H. Rivett, G. Nan, G. D. Tainter, T. A. S. Doherty, K. Frohna, E. Ringe, R. H. Friend, H. Sirringhaus, M. Saliba, D. Beljonne, S. D. Stranks, F. Deschler, *Nat. Photonics* **2020**, *14*, 123.

[11] C. M. Wolff, P. Caprioglio, M. Stolterfoht, D. Neher, *Adv. Mater.* **2019**, *31*, 1902762.

[12] M. J. Trimpl, A. D. Wright, K. Schutt, L. R. V. Buizza, Z. Wang, M. B. Johnston, H. J. Snaith, P. Müller-Buschbaum, L. M. Herz, *Adv. Funct. Mater.* **2020**, *30*, 2004312.

[13] K. Frohna, M. Anaya, S. Macpherson, J. Sung, T. A. S. Doherty, Y. H. Chiang, A. J. Winchester, K. W. P. Orr, J. E. Parker, P. D. Quinn, K. M. Dani, A. Rao, S. D. Stranks, *Nat. Nanotechnol.* **2022**, *17*, 190.

[14] T. A. S. Doherty, A. J. Winchester, S. Macpherson, D. N. Johnstone, V. Pareek, E. M. Tennyson, S. Kosar, F. U. Kosasih, M. Anaya, M. Abdi-Jalebi, Z. Andaji-Garmaroudi, E. L. Wong, J. Madéo, Y. H. Chiang, J. S. Park, Y. K. Jung, C. E. Petoukhoff, G. Divitini, M. K. L. Man, C. Ducati, A. Walsh, P. A. Midgley, K. M. Dani, S. D. Stranks, *Nature* **2020**, *580*, 360.

[15] R. A. Belisle, W. H. Nguyen, A. R. Bowring, P. Calado, X. Li, S. J. C. Irvine, M. D. McGehee, P. R. F. Barnes, B. C. O'Regan, *Energy Environ. Sci.* **2017**, *10*, 192.

[16] P. Calado, A. M. Telford, D. Bryant, X. Li, J. Nelson, B. C. O'Regan, P. R. F. Barnes, *Nat. Commun.* **2016**, *7*, 13831.

[17] L. Bertoluzzi, R. A. Belisle, K. A. Bush, R. Cheacharoen, M. D. McGehee, B. C. O'Regan, *J. Am. Chem. Soc.* **2018**, *140*, 12775.

[18] T. Zhang, H. Chen, Y. Bai, S. Xiao, L. Zhu, C. Hu, Q. Xue, S. Yang, *Nano Energy* **2016**, *26*, 620.

**ADVANCED
SCIENCE NEWS**

www.advancedsciencenews.com

**ADVANCED
ENERGY
MATERIALS**

www.advenergymat.de

[19] B. Chen, M. Yang, X. Zheng, C. Wu, W. Li, Y. Yan, J. Bisquert, G. Garcia-Belmonte, K. Zhu, S. Priya, *J. Phys. Chem. Lett.* **2015**, *6*, 4693.

[20] C. Zhao, B. Chen, X. Qiao, L. Luan, K. Lu, B. Hu, *Adv. Energy Mater.* **2015**, *5*, 1500279.

[21] X. Deng, X. Wen, J. Zheng, T. Young, C. F. J. Lau, J. Kim, M. Green, S. Huang, A. Ho-Baillie, *Nano Energy* **2018**, *46*, 356.

[22] J. Thiesbrummel, V. M. Le Corre, F. Peña-Camargo, L. Perdigón-Toro, F. Lang, F. Yang, M. Grischek, E. Gutierrez-Partida, J. Warby, M. D. Farrar, S. Mahesh, P. Caprioglio, S. Albrecht, D. Neher, H. J. Snaith, M. Stolterfoht, *Adv. Energy Mater.* **2021**, *11*, 2101447.

[23] S. A. L. Weber, I. M. Hermes, S. H. Turren-Cruz, C. Gort, V. W. Bergmann, L. Gilson, A. Hagfeldt, M. Graetzel, W. Tress, R. Berger, *Energy Environ. Sci.* **2018**, *11*, 2404.

[24] P. Calado, D. Burkitt, J. Yao, J. Troughton, T. M. Watson, M. J. Carnie, A. M. Telford, B. C. O'Regan, J. Nelson, P. R. F. Barnes, *Phys. Rev. Appl.* **2019**, *11*, 044005.

[25] J. Warby, F. Zu, S. Zeiske, E. Gutierrez-Partida, L. Frohloff, S. Kahmann, K. Frohna, E. Mosconi, E. Radicchi, F. Lang, S. Shah, F. Peña-Camargo, H. Hempel, T. Unold, N. Koch, A. Armin, F. De Angelis, S. D. Stranks, D. Neher, M. Stolterfoht, *Adv. Energy Mater.* **2022**, *12*, 2103567.

[26] Y. Fang, C. Bi, D. Wang, J. Huang, *ACS Energy Lett.* **2017**, *2*, 782.

[27] R. D. J. Oliver, P. Caprioglio, F. Peña-Camargo, L. R. V. Buizza, F. Zu, A. J. Ramadan, S. G. Motti, S. Mahesh, M. M. McCarthy, J. H. Warby, Y. H. Lin, N. Koch, S. Albrecht, L. M. Herz, M. B. Johnston, D. Neher, M. Stolterfoht, H. J. Snaith, *Energy Environ. Sci.* **2022**, *15*, 714.

[28] Y. Tong, A. Najar, L. Wang, L. Liu, M. Du, J. Yang, J. Li, K. Wang, S. Liu, *Adv. Sci.* **2022**, *9*, 2105085.

[29] S. H. Turren-Cruz, A. Hagfeldt, M. Saliba, *Science* **2018**, *362*, 449.

[30] X. X. Gao, W. Luo, Y. Zhang, R. Hu, B. Zhang, A. Züttel, Y. Feng, M. K. Nazeeruddin, *Adv. Mater.* **2020**, *32*, 1905502.

[31] S. Gharibzadeh, P. Fassl, I. M. Hossain, P. Rohrbeck, M. Frericks, M. Schmidt, T. Duong, M. R. Khan, T. Abzieher, B. A. Nejand, F. Schackmar, O. Almora, T. Feeney, R. Singh, D. Fuchs, U. Lemmer, J. P. Hofmann, S. A. L. Weber, U. W. Paetzold, *Energy Environ. Sci.* **2021**, *14*, 5875.

[32] Y. H. Lin, N. Sakai, P. Da, J. Wu, H. C. Sansom, A. J. Ramadan, S. Mahesh, J. Liu, R. D. J. Oliver, J. Lim, L. Aspitarte, K. Sharma, P. K. Madhu, A. B. Morales-Vilches, P. K. Nayak, S. Bai, F. Gao, C. R. M. Grovenor, M. B. Johnston, J. G. Labram, J. R. Durrant, J. M. Ball, B. Wenger, B. Stannowski, H. J. Snaith, *Science* **2020**, *369*, 96.

[33] P. Caprioglio, M. Stolterfoht, C. M. Wolff, T. Unold, B. Rech, S. Albrecht, D. Neher, *Adv. Energy Mater.* **2019**, *9*, 1901631.

[34] T. Du, W. Xu, M. Daboczi, J. Kim, S. Xu, C. T. Lin, H. Kang, K. Lee, M. J. Heeney, J. S. Kim, J. R. Durrant, M. A. McLachlan, *J. Mater. Chem. A* **2019**, *7*, 18971.

[35] T. Du, W. Xu, S. Xu, S. R. Ratnasingham, C. T. Lin, J. Kim, J. Briscoe, M. A. McLachlan, J. R. Durrant, *J. Mater. Chem. C* **2020**, *8*, 12648.

[36] U. Rau, *Phys. Rev. B* **2007**, *76*, 085303.

[37] Z. Liu, L. Krückemeier, B. Krogmeier, B. Klingebiel, J. A. Márquez, S. Levcenko, S. Öz, S. Mathur, U. Rau, T. Unold, T. Kirchartz, *ACS Energy Lett.* **2019**, *4*, 110.

[38] M. Stolterfoht, P. Caprioglio, C. M. Wolff, J. A. Márquez, J. Nordmann, S. Zhang, D. Rothhardt, U. Hörmann, Y. Amir, A. Redinger, L. Kegelmann, F. Zu, S. Albrecht, N. Koch, T. Kirchartz, M. Saliba, T. Unold, D. Neher, *Energy Environ. Sci.* **2019**, *12*, 2778.

[39] X. Ling, H. Zhu, W. Xu, C. Liu, L. Pan, D. Ren, J. Yuan, B. W. Larson, C. Grätzel, A. R. Kirmani, O. Ouellette, A. Krishna, J. Sun, C. Zhang, Y. Li, S. M. Zakeeruddin, J. Gao, Y. Liu, J. R. Durrant, J. M. Luther, W. Ma, M. Grätzel, *Angew. Chem., Int. Ed.* **2021**, *60*, 27299.

[40] T. J. MacDonald, A. J. Clancy, W. Xu, Z. Jiang, C. T. Lin, L. Mohan, T. Du, D. D. Tune, L. Lanzetta, G. Min, T. Webb, A. Ashoka, R. Pandya, V. Tileli, M. A. McLachlan, J. R. Durrant, S. A. Haque, C. A. Howard, *J. Am. Chem. Soc.* **2021**, *143*, 21549.

[41] A. Dasgupta, S. Mahesh, P. Caprioglio, Y.-H. Lin, K.-A. Zaininger, R. D. J. Oliver, P. Holzhey, S. Zhou, M. M. McCarthy, J. A. Smith, M. Frenzel, M. G. Christoforo, J. M. Ball, B. Wenger, H. J. Snaith, *ACS Energy Lett.* **2022**, *7*, 2311.

[42] C. Dreessen, D. Pérez-del-Rey, P. P. Boix, H. J. Bolink, *J. Lumin.* **2020**, *222*, 117106.

[43] L. Wagner, P. Schygulla, J. P. Herterich, M. Elshamy, D. Bogachuk, S. Zouhair, S. Mastroianni, U. Würfel, Y. Liu, S. M. Zakeeruddin, M. Grätzel, A. Hinsch, S. W. Glunz, *Matter* **2022**, *5*, 2352.

[44] R. E. M. Willems, S. C. J. Meskers, M. M. Wienk, R. A. J. Janssen, *J. Phys. Chem. C* **2019**, *123*, 10253.

[45] F. C. Jamieson, E. B. Domingo, T. Mccarthy-Ward, M. Heeney, N. Stingelin, J. R. Durrant, *Chem. Sci.* **2012**, *3*, 485.

[46] Y. Shao, Y. Yuan, J. Huang, *Nat. Energy* **2016**, *1*, 15001.

[47] Y. Lin, B. Chen, F. Zhao, X. Zheng, Y. Deng, Y. Shao, Y. Fang, Y. Bai, C. Wang, J. Huang, *Adv. Mater.* **2017**, *29*, 1700607.

[48] C. G. Wu, C. H. Chiang, S. H. Chang, *Nanoscale* **2016**, *8*, 4077.

[49] L. Gil-Escrig, C. Momblona, M. Sessolo, H. J. Bolink, *J. Mater. Chem. A* **2016**, *4*, 3667.

[50] M. S. Vezie, M. Azzouzi, A. M. Telford, T. R. Hopper, A. B. Sieval, J. C. Hummelen, K. Fallon, H. Bronstein, T. Kirchartz, A. A. Bakulin, T. M. Clarke, J. Nelson, *ACS Energy Lett.* **2019**, *4*, 2096.

[51] H. Hu, S. Moghadamzadeh, R. Azmi, Y. Li, M. Kaiser, J. C. Fischer, Q. Jin, J. Maibach, I. M. Hossain, U. W. Paetzold, B. Abdollahi, H. Hu, S. Moghadamzadeh, Y. Li, M. Kaiser, J. C. Fischer, I. M. Hossain, U. W. Paetzold, B. A. Nejand, *Adv. Funct. Mater.* **2021**, *32*, 2107650.

[52] L. L. Deng, S. Y. Xie, F. Gao, *Adv. Electron. Mater.* **2018**, *4*, 1700435.

[53] J. A. Röhr, D. Moia, S. A. Haque, T. Kirchartz, J. Nelson, *J. Phys.: Condens. Matter* **2018**, *30*, 105901.

[54] F. M. Rombach, S. A. Haque, T. J. Macdonald, *Energy Environ. Sci.* **2021**, *14*, 5161.

[55] S. Liu, R. Chen, X. Tian, Z. Yang, J. Zhou, F. Ren, S. Zhang, Y. Zhang, M. Guo, Y. Shen, Z. Liu, W. Chen, *Nano Energy* **2022**, *94*, 106935.

[56] R. Chen, S. Liu, X. Xu, F. Ren, J. Zhou, X. Tian, Z. Yang, X. Guanz, Z. Liu, S. Zhang, Y. Zhang, Y. Wu, L. Han, Y. Qi, W. Chen, *Energy Environ. Sci.* **2022**, *15*, 2567.

[57] D. J. Slotcavage, H. I. Karunadasa, M. D. McGehee, *ACS Energy Lett.* **2016**, *1*, 1199.

[58] T. Zhang, S. H. Cheung, X. Meng, L. Zhu, Y. Bai, C. H. Y. Ho, S. Xiao, Q. Xue, S. K. So, S. Yang, *J. Phys. Chem. Lett.* **2017**, *8*, 5069.

[59] J. Herterich, M. Unmüssig, G. Loukeris, M. Kohlstädt, U. Würfel, *Energy Technol.* **2021**, *9*, 2001104.

[60] P. Calado, I. Gelmetti, B. Hilton, M. Azzouzi, J. Nelson, P. R. F. Barnes, *J. Comput. Electron.* **2022**, *21*, 960.

[61] I. M. Hermes, Y. Hou, V. W. Bergmann, C. J. Brabec, S. A. L. Weber, *J. Phys. Chem. Lett.* **2018**, *21*, 6249.

[62] D. Moia, I. Gelmetti, P. Calado, Y. Hu, X. Li, P. Docampo, J. De Mello, J. Maier, J. Nelson, P. R. F. Barnes, *Phys. Rev. Appl.* **2022**, *18*, 044056.

[63] V. M. Le Corre, J. Diekmann, F. Peña-Camargo, J. Thiesbrummel, N. Tokmoldin, E. Gutierrez-Partida, K. P. Peters, L. Perdigón-Toro, M. H. Futscher, F. Lang, J. Warby, H. J. Snaith, D. Neher, M. Stolterfoht, *Sol. RRL* **2022**, *6*, 2100772.

[64] J. Nelson, *The Physics of Solar Cells*, Imperial College Press, London **2003**.

[65] D. E. Carlson, *Sol. Energy Mater.* **1980**, *3*, 503.

[66] V. M. Le Corre, M. Stolterfoht, L. Perdigón Toro, M. Feuerstein, C. Wolff, L. Gil-Escrig, H. J. Bolink, D. Neher, L. J. A. Koster, *ACS Appl. Energy Mater.* **2019**, *2*, 6280.

[67] S. Akel, A. Kulkarni, U. Rau, T. Kirchartz, *PRX Energy* **2023**, *2*, 013004.

[68] B. C. O'Regan, J. R. Durrant, P. M. Sommeling, N. J. Bakker, *J. Phys. Chem. C* **2007**, *111*, 14001.

[69] C. G. Shuttle, R. Hamilton, J. Nelson, B. C. O'Regan, J. R. Durrant, *Adv. Funct. Mater.* **2010**, *20*, 698.

[70] J. Wu, H. Cha, T. Du, Y. Dong, W. Xu, C. T. Lin, J. R. Durrant, *Adv. Mater.* **2022**, *34*, 2101833.

[71] R. E. Hollingsworth, J. R. Sites, *J. Appl. Phys.* **1984**, *56*, 3451.

[72] U. Rau, V. Huhn, B. E. Pieters, *Phys. Rev. Appl.* **2020**, *14*, 014046.

[73] P. Caprioglio, C. M. Wolff, O. J. Sandberg, A. Armin, B. Rech, S. Albrecht, D. Neher, M. Stolterfoht, *Adv. Energy Mater.* **2020**, *10*, 2000502.

[74] T. Chen, Z. Sun, M. Liang, S. Xue, *Phys. Chem. Chem. Phys.* **2019**, *22*, 245.

[75] A. Magomedov, A. Al-Ashouri, E. Kasparavičius, S. Strazdaite, G. Niaura, M. Jošt, T. Malinauskas, S. Albrecht, V. Getautis, *Adv. Energy Mater.* **2018**, *8*, 1801892.

[76] E. Aktas, N. Phung, H. Köbler, D. A. González, M. Méndez, I. Kafedjiska, S. H. Turren-Cruz, R. Wenisch, I. Lauermann, A. Abate, E. Palomares, *Energy Environ. Sci.* **2021**, *14*, 3976.

[77] A. Al-Ashouri, E. Köhnen, B. Li, A. Magomedov, H. Hempel, P. Caprioglio, J. A. Márquez, A. B. M. Vilches, E. Kasparavicius, J. A. Smith, N. Phung, D. Menzel, M. Grischek, L. Kegelmann, D. Skroblin, C. Gollwitzer, T. Malinauskas, M. Jošt, G. Matič, B. Rech, R. Schlatmann, M. Topič, L. Korte, A. Abate, B. Stannowski, D. Neher, M. Stolterfoht, T. Unold, V. Getautis, S. Albrecht, *Science* **2020**, *370*, 1300.

[78] A. Al-Ashouri, A. Magomedov, M. Roß, M. Jošt, M. Talaikis, G. Chistiakova, T. Bertram, J. A. Márquez, E. Köhnen, E. Kasparavičius, S. Levcenco, L. Gil-Escrig, C. J. Hages, R. Schlatmann, B. Rech, T. Malinauskas, T. Unold, C. A. Kaufmann, L. Korte, G. Niaura, V. Getautis, S. Albrecht, *Energy Environ. Sci.* **2019**, *12*, 3356.